JINR Summer Student Program 2014

Study of the experiment BM@N: material budget and physics analysis

Diana Leyva Pernia

Summary:

BM@N (Baryonic Matter at Nuclotron) is an experimental setup to perform a research program focused on the production of strange matter in heavy-ion collisions. The first measurements are planned for 2015, but there are already some studies performed through mathematical simulations that will contribute to the proper comprehension of future experimental results. In this work the structure of both detector system and events to be obtained at BM@N was analyzed. The correct understanding of the material quantity in the components of the detection system is extremely important for obtaining an accurate particle reconstruction performance and insights of events structure could provide a useful guidance for further studies in this field of science.

1. Detector Structure

Mapping the material is usually a fundamental task at the beginning of data acquisition in HEP experiments. The proper understanding of the material quantity in components of the detection system is crucial for obtaining an accurate particle reconstruction performance.

The use of simulation as a first step in accomplishing this task is a very helpful and conventional practice. Mapping with actual experimental data requires a considerable amount of time and simulations can supply the necessary information to quantify detection possibilities even before the detection system is fully assembled. Furthermore, the study of the material budget is also advantageous for checking the system geometry built for the simulations.

In this project the detector structure of BM@N is studied by making use of BmnRoot framework, both for the simulation and analysis tasks. The simulations were performed using Geant3 toolkit for the transport of particles through matter.

The BM@N experimental setup includes a large-acceptance dipole magnet with inner tracking detector modules based on double-sided silicon micro-strip sensors and gaseous detectors (GEMs). The outer tracking will be based on drift chambers (DCH), time of flight system (TOF) and zero degree calorimeter (ZDC). In Figure 1.1 is shown a schematic representation of the complete system.

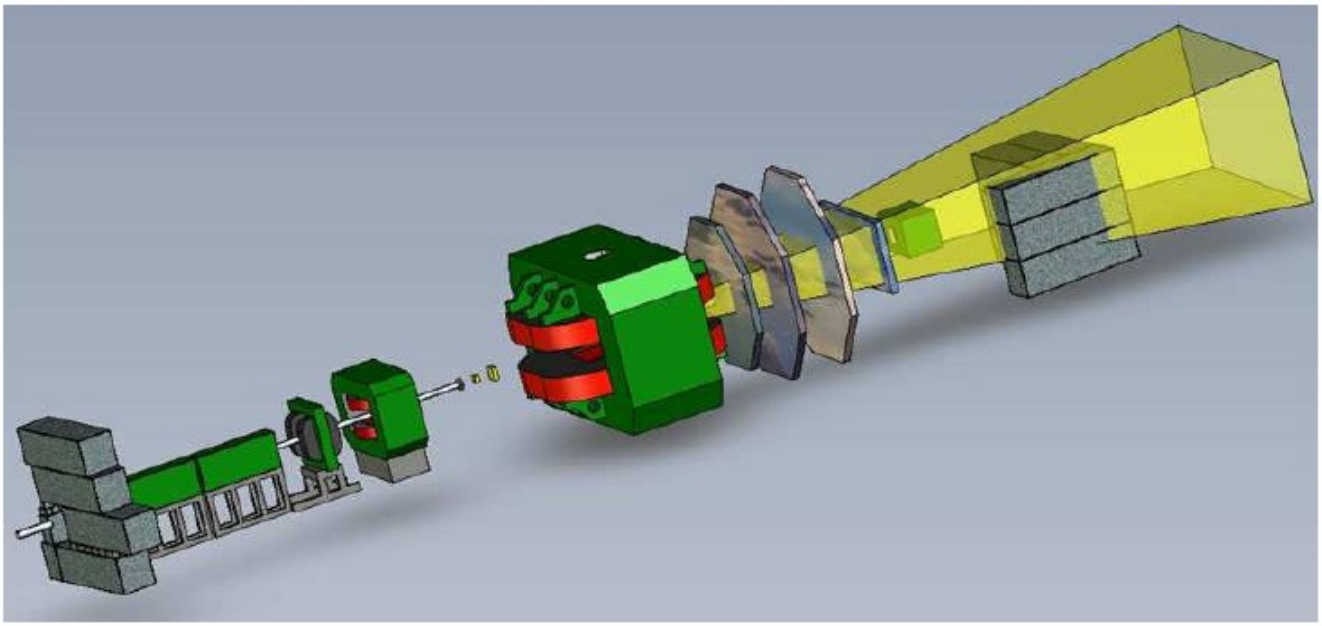

Fig. 1.1: *Schematic representation of BM@N.*

Meanwhile the project is doing, task of implementing the BM@N geometry for simulations is being performed. Therefore, it was possible to study the components already completed listed in table 1.1. The schematic representation of these components is displayed in the figure 1.2.

Table. 1.1: *Components of BM@N system included in this study.*

	SYSTEM ELEMENTS
1	Target
2	Beam Pipe
3	Magnets
4	Recoil Detector
5	GEMs (12 Gas Electron Multiplier trackers)
6	ToF1 (1^{st} Time of Flight detector)
7	DCH1 (1^{st} Drift Chamber)
8	DCH2 (2^{nd} Drift Chamber)
9	ToF2 (2^{nd} Time of Flight detector)
10	ZDC (Zero Degree Calorimeter)

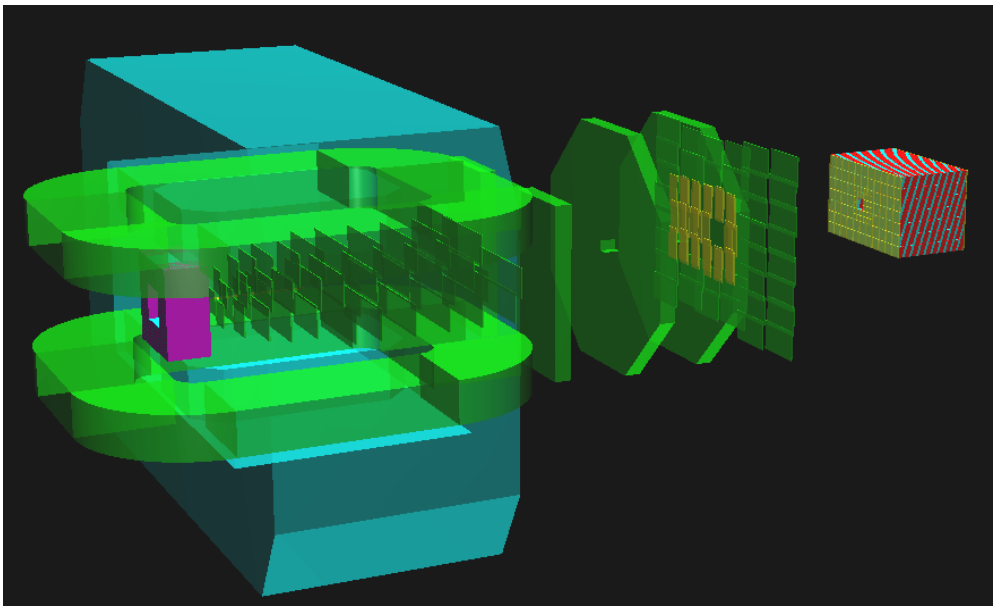

Fig. 1.2: *Schematic representation of the analyzed system.*

A standard way to obtain the material distribution of a detection system is realized by performing a geantino scan. Geantinos are virtual particles constructed by Geant toolkit. These particles do not interact with matter and undertake transportation processes only carrying information about the geometry they have traversed.

Using this procedure the first approximation of the material budget for BM@N was obtained and the results are presented in the figures 1.3 and 1.4. In those figures the information about material distribution for the XZ and YZ planes is respectively displayed.

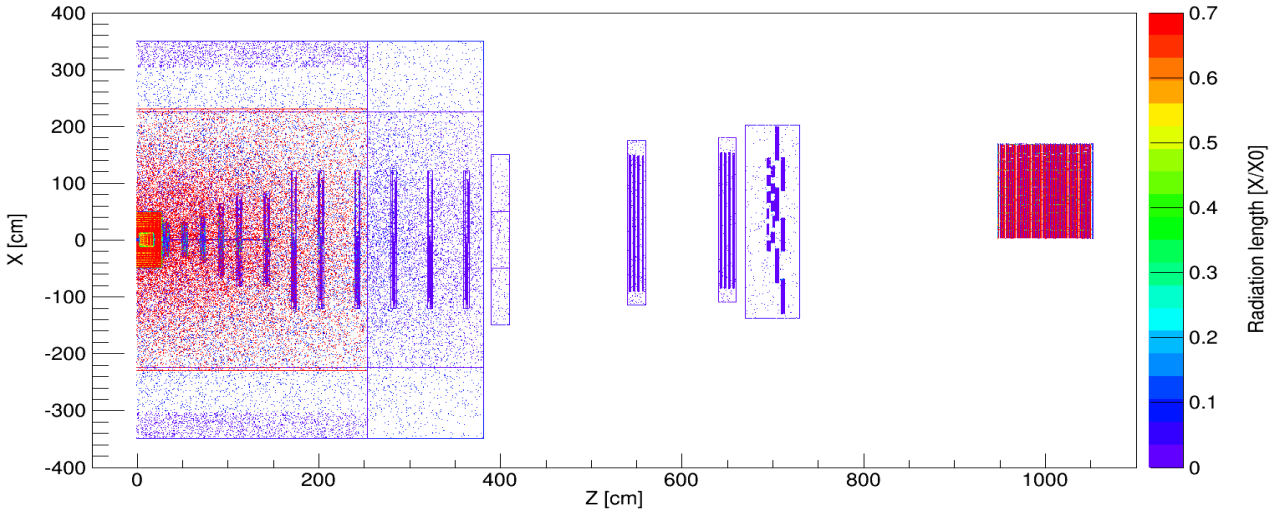

Fig. 1.3: *Integrated material budget at the XZ plane.*

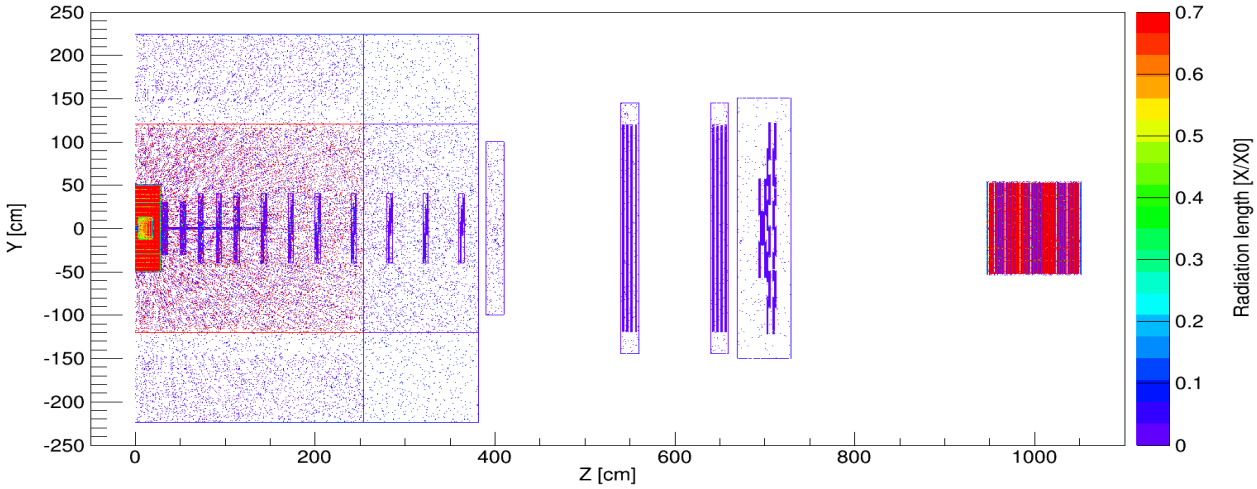

Fig. 1.4: *Integrated material budget at the YZ plane.*

In the both cases it is possible to identify different components of the system, their structure and the areas where the material budget is highest. The areas where the radiation length reaches values of approximately 0.65 and 0.7 correspond to the location of the ZDC, the central region of the magnet, the recoil detector and, apparently, the target and the first section of the beam pipe. Due to the overlapping projections of the different system components placed inside the magnet (recoil detector, target, beam pipe and GEMs) the differentiation of the radiation length reached by the geantinos in each of them is not correctly appreciated.

The next step in study of the system structure consisted in obtaining the material budget as a function of pseudorapidity η. For this purpose a new simulation where the geantinos were transported through the system along a central line with η values in the span from -1 up to 7 was performed. The image obtained is presented in figure 1.5.

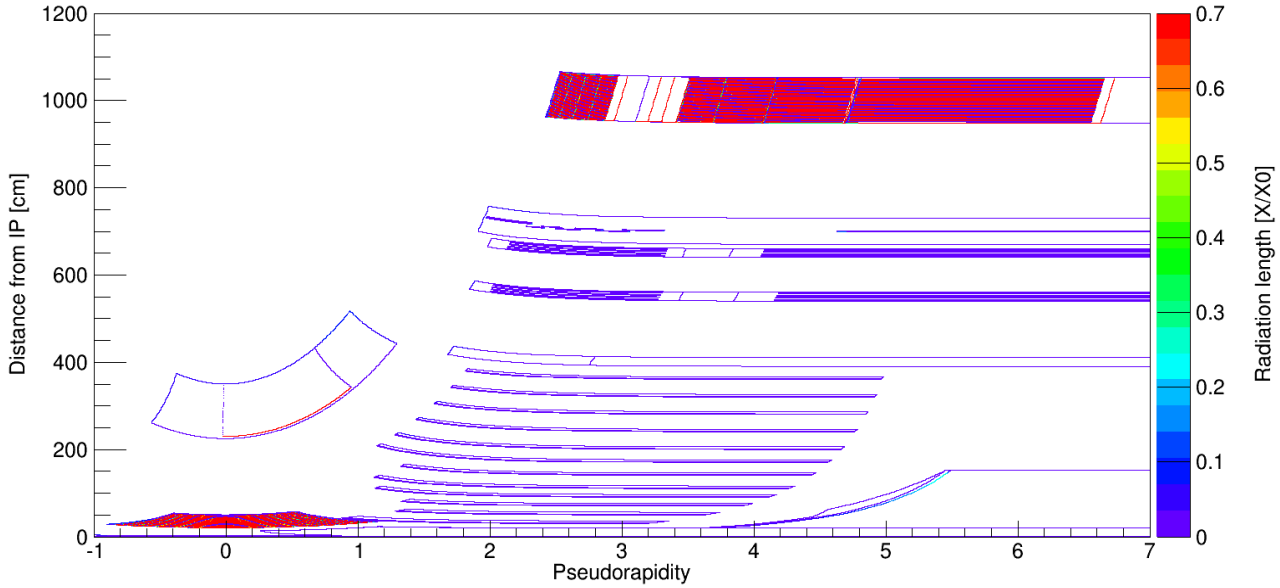

Fig. 1.5: *Material distribution at the plane conformed between the distance from the interaction point and the pseudorapidity.*

In this figure it is now possible to appreciate the inner structure of the ZDC, TOF2 and both of the DCH detectors. It is also feasible to identify the GEMs and the recoil detector structures without overlapping the magnet. Nevertheless, it is still not possible to recognize the target and beam pipe contribution in the area inside the recoil detector. The previous case the highest values of radiation length can be found at the ZDC, the magnet and the recoil detector. Now it could be stated that in the magnet the highest values are only reached in the lower inner region.

When the integrated radiation length is analyzed as a function of the pseudorapidity (figure 1.6) the results obtained are consistent with the expected behavior. For the range of pseudorapidity comprehended between -1 and 0 the high values of radiation length achieved correspond to the presence of the recoil detector, while the increment observed in the region from 0 to 1 corresponds to sector, where the detector is overlapped with the magnet. It is also feasible to identify the region comprehending the ZDC contribution in the interval from 2.4 to 6.6. For the rest of the system components the corresponding contribution is not so obvious to identify. The region of pseudorapidity between 1 and 2 should include mainly the information related to the GEMs, but for higher values the resultant information comes from superposition of contributions of the GEMs, both TOF and both DCH.

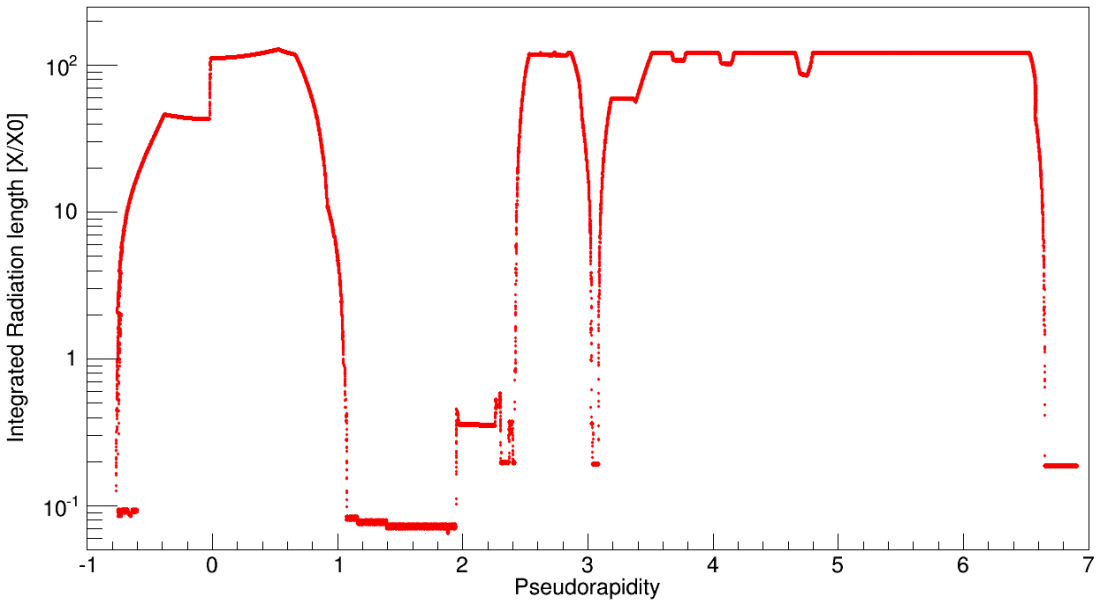

Fig. 1.6: *Integrated radiation length as a function of pseudorapidity.*

In order to get a proper knowledge of the actual contribution of each system component to the radiation length a new set of simulations was performed. The elements were analyzed individually and the background information coming from the experiment cave was removed. The results obtained are presented in the figure 1.7.

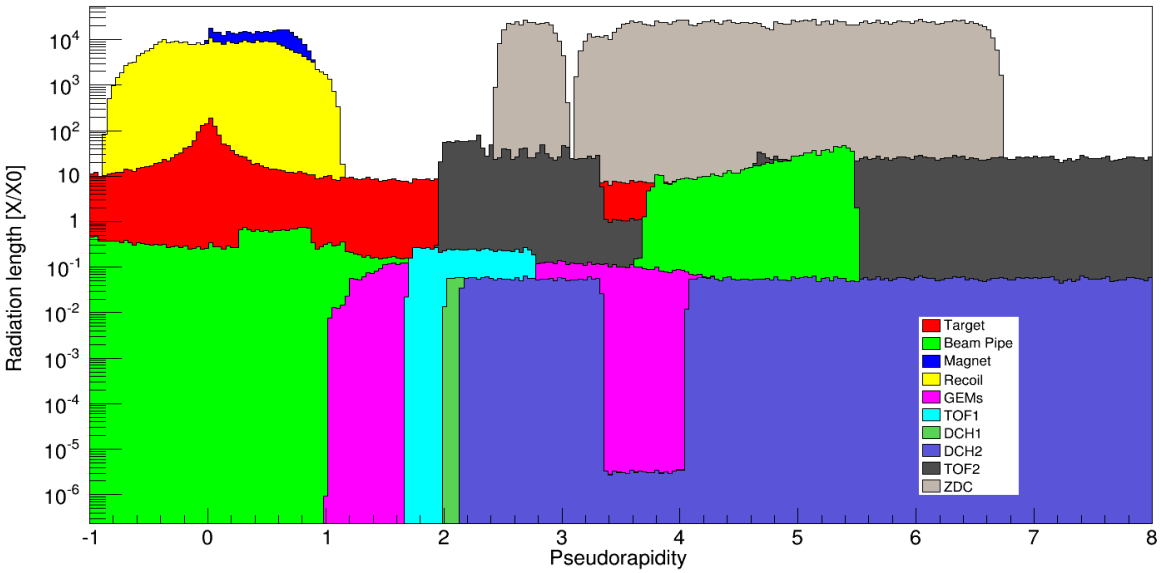

Fig. 1.7: *Radiation length as a function of pseudorapidity.*

Another way to find the material distribution is realized by performing electron-positron pair scans. Since the pair production cross section can be considered directly proportional to the square of the atomic number, the regions where increased production of pairs is detected can be linked to the presence of heavier materials. Figure 1.8 shows the results obtained from two cases, one in which the direct gamma pair production was only considered, and other where all electron-positron pairs were collected.

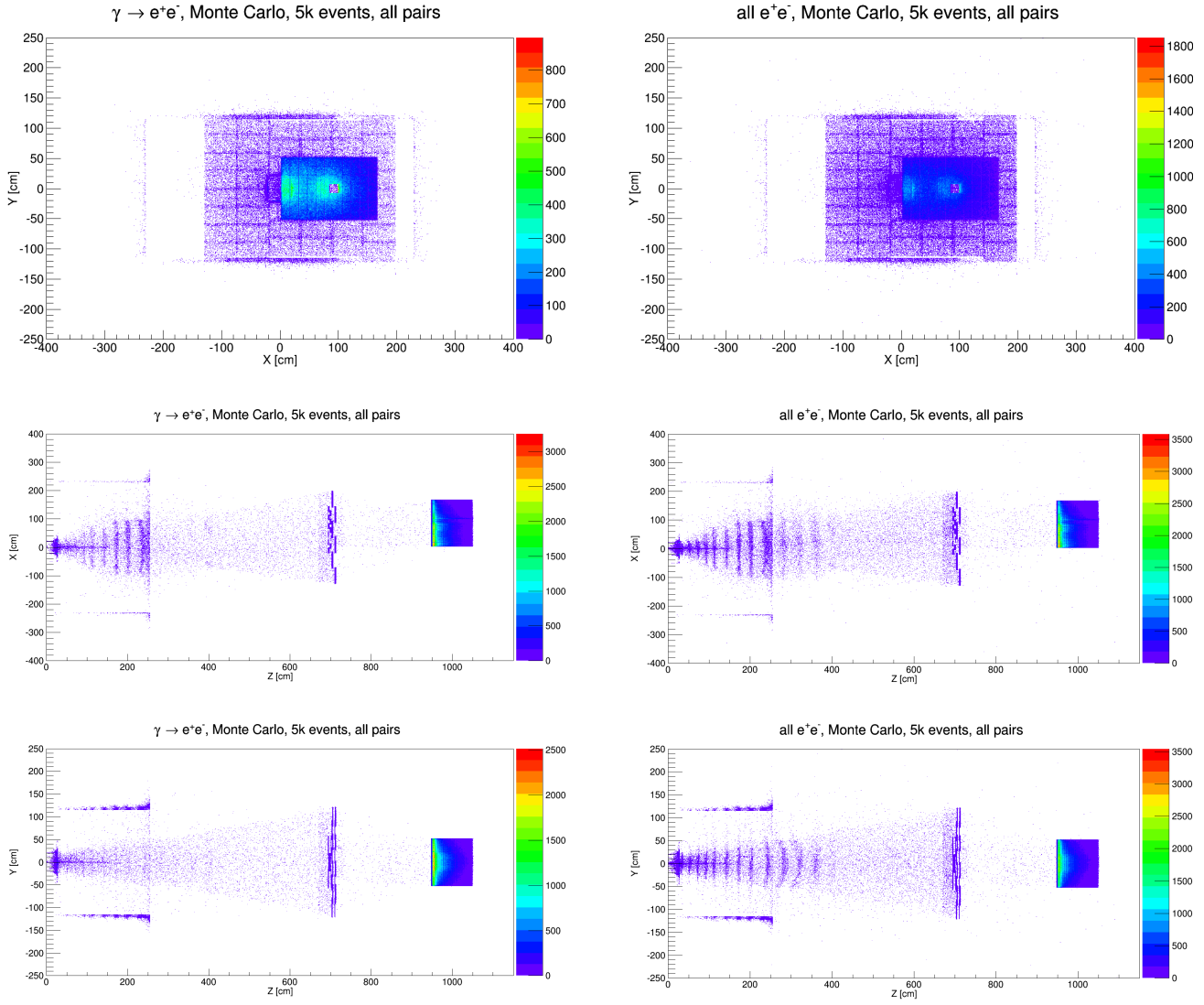

Fig. 1.8: *Different projections of the pair production scans.*

In the both scenarios the largest number of the pair productions was found at the ZDC and it was possible to observe the internal layered structure of the TOF2. However, it was not possible to identify the presence of the TOF1, DCH1 and DCH2 detectors. In the XZ and YZ projections it can also be observed the recoil detector, the beam pipe and inner structure of the magnet. Despite their similarity, here are noticeable differences between two set of images presented. In case, when all the electron-positron pairs were collected a larger number of events was recorded and the GEMs were more clearly identified.

2. Event Structure

Event shape variables describe structure of the energy flow in QCD events. With these variables is possible to distinguish different configurations, in which the energy is distributed uniformly over the 4π-solid angle and those, where dijet events occur. The sphericity S defined by formula (2.1), is a widely used event shape variable which describes the event energy flow based on the momentum tensor.

$$S^{\alpha\beta} = \frac{\sum_i P_i^{\alpha} P_i^{\beta}}{\sum_i \left|\vec{P}_i\right|^2} \tag{2.1}$$

The sphericity has values between 0 and 1, where isotropic events corresponds to $S=1$ and the pencil-like events corresponds to $S=0$.

Transverse sphericity S_T is expressed in terms of the transverse components only (2.3) and it is defined in terms of the eigenvalues λ_1 and λ_2, where $\lambda_1 > \lambda_2$.

$$S_T = \frac{\sum_i P_i^x P_i^y}{\sum_i |\vec{P}_{Ti}|^2} = \sum_i \frac{1}{|\vec{P}_{Ti}|^2} \begin{bmatrix} P_i^x P_i^x & P_i^x P_i^y \\ P_i^x P_i^y & P_i^y P_i^y \end{bmatrix} \tag{2.2}$$

$$S_T = \frac{2\lambda_2}{\lambda_1 + \lambda_2} \tag{2.3}$$

Figure 2.1 shows the histogram obtained from the transverse sphericity in a minimum bias Au-Au collision at energy E = 11 GeV/nucleon. The distribution corresponds to the one expected, where the most probable value of transverse sphericity is around 0.95 and in the both limits (0 and 1) tends to 0.

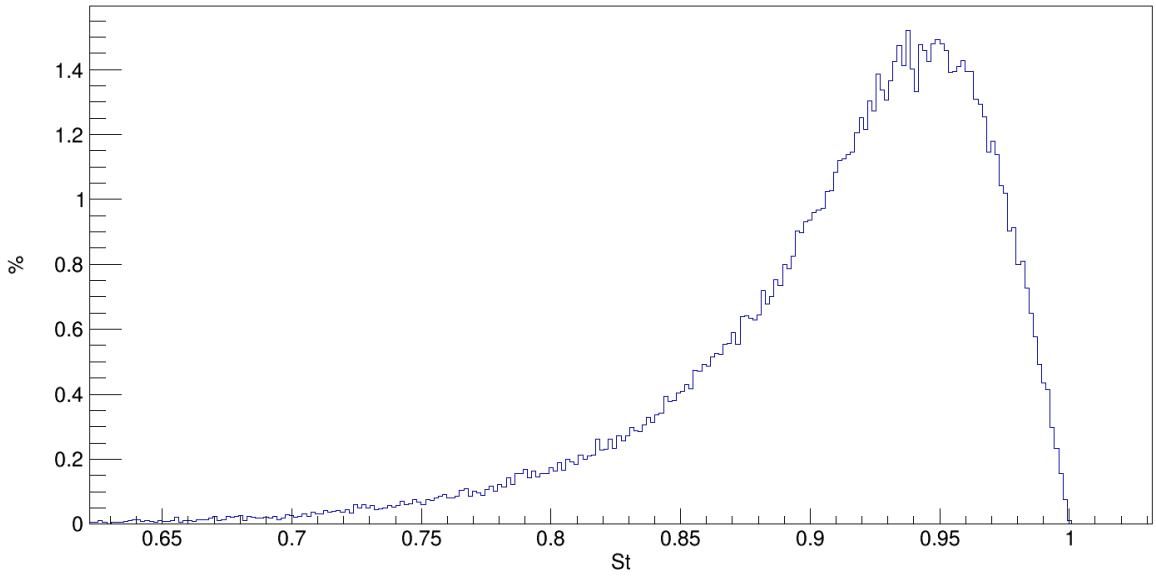

Fig. 2.1: *Transverse Sphericity.*

For the same case, the transverse momentum Pt versus the maximum Pt distribution (figure 2.2) was also plotted. In this figure one can detect a region corresponding to anisotropic events for Pt max values larger than 2.5 GeV/c.

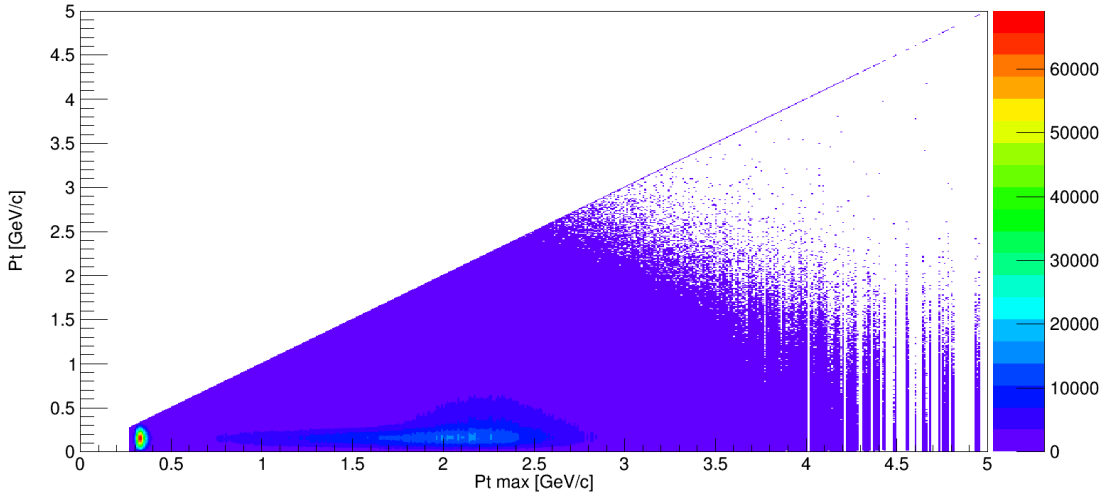

Fig. 2.2: *Transverse momentum distribution as a function of the maximum transverse momentum.*

It would be interesting to check if any direct relations could be found between S_T and the Pt max (figure 2.3).

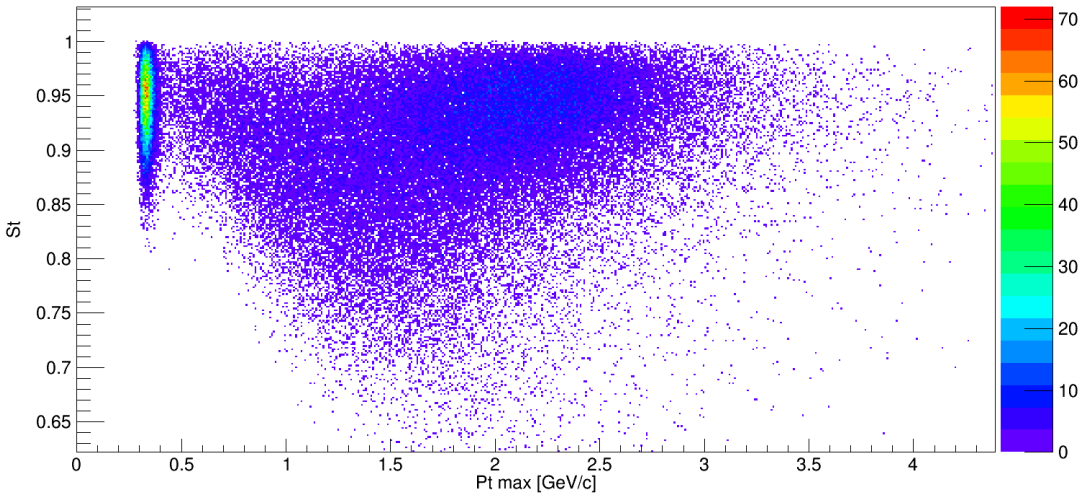

Fig. 2.3: *Transverse sphericity vs maximum transverse momentum.*

The image obtained corresponds to a scatter-plot distribution showing a possibility of getting more than one event with equal or very similar values of Pt max and the different corresponding values of the transverse sphericity. From this graph cannot be discerned any specific pattern that would allow to identify the presence of the anisotropic events. Therefore, it was also analyzed the behavior of the average transverse sphericity. The results obtained are shown in the figure 2.4, where is displayed the mean value of the transverse sphericity and its error for each bin of Pt max.

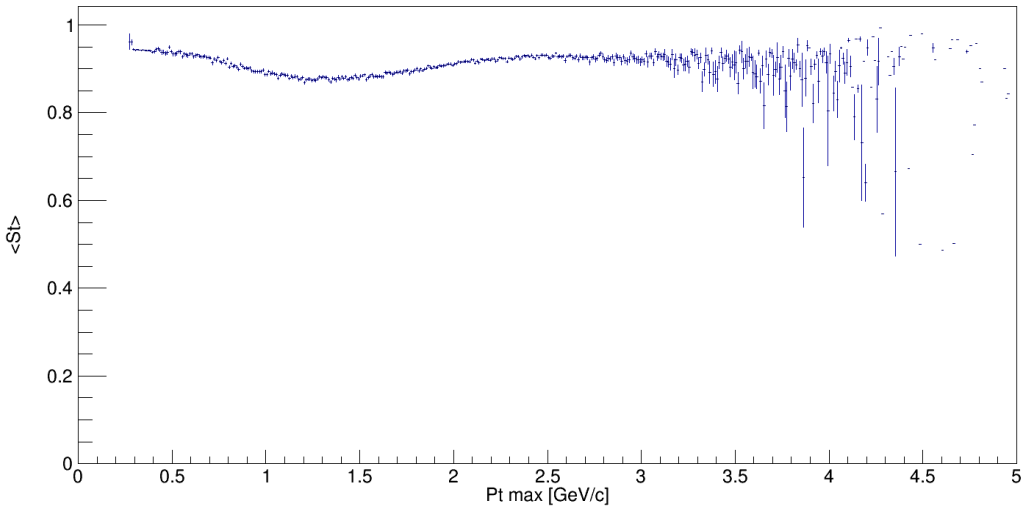

Fig. 2.4: Mean value of transverse sphericity vs maximum transverse momentum.

In this graph a clear decrease of the mean S_t values after reaching the Pt max larger than 2.5 GeV/c as a result of the pencil-like shape of anisotropic events was expected to observe. However, for that specific region of Pt max the results obtained have a considerably high relative error and there is a remarkable dispersion between the plotted points. This is probably due to low number of events obtained for these Pt max values. So, it would be necessary to increase the number of events simulated in order to achieve better statistics.

To reduce the contribution from beam-related backgrounds and to minimize systematic uncertainties, the mean value of St as a function of Pt max obtained from different cuts on Pt and/or η or a combination of the both of them, was built (figure 2.5). Although the graphics obtained showed a change in the behavior of the *St* for the lowest values of Pt max, in the region of interest the lack of appropriate statistics does not allow us to arrive at any definite conclusion.

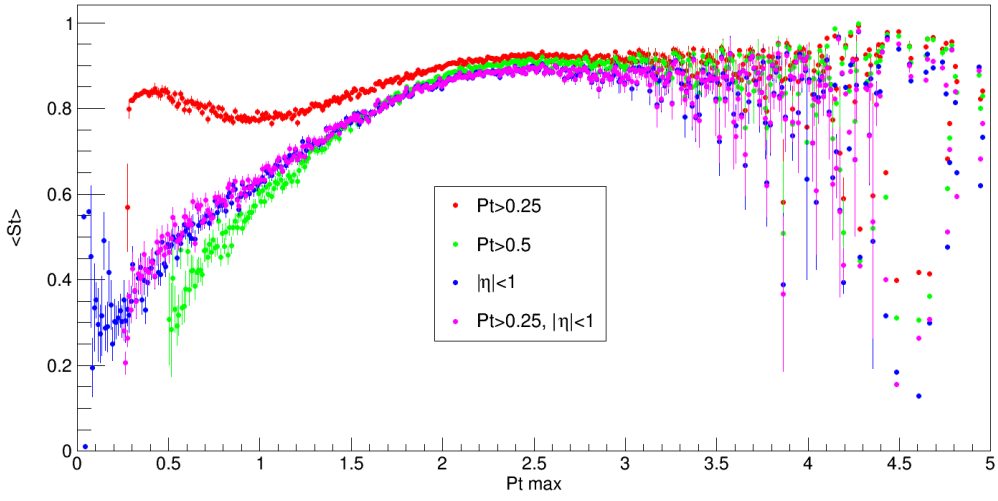

Fig. 2.5: Mean value of St as a function of Pt max obtained from different cuts on Pt and/or η.

Applying the cuts mentioned above, the behavior of the mean Pt value as a function of Pt max was analyzed (figure 2.6). In the figure one can observe how the mean Pt increases with Pt max reaching plateau at a given value of Pt max for different cuts.

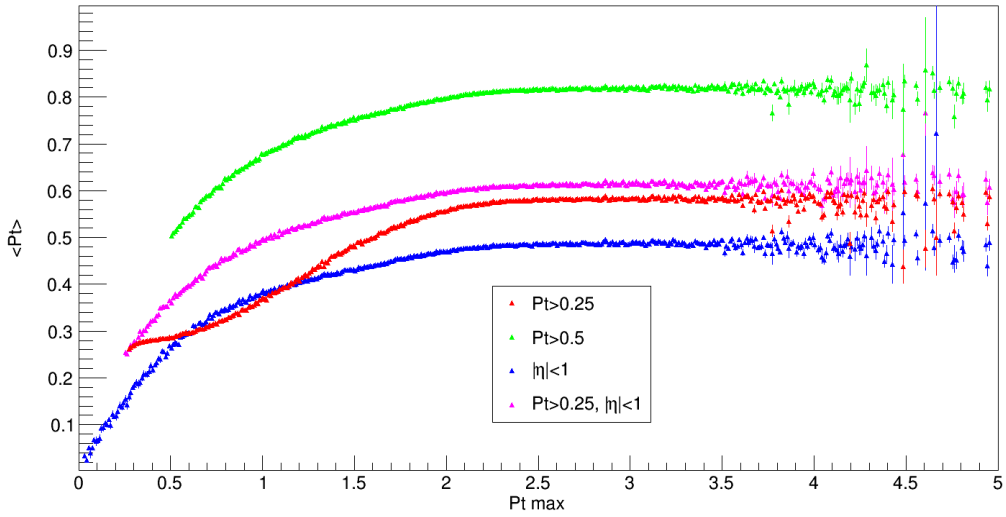

Fig. 2.6: Mean value of Pt as a function of Pt max for different cuts of Pt and/or η.

The maximum value of the mean Pt reached is different for each individual cuts made. However, it is always reached around the same value of Pt max, which corresponds to the appearance of anisotropic events.

In the figure 2.7 the mean S_t is shown as a function of the mean Pt. The graph shows that <St> increases with <Pt> until the last reaches the value, where the plateau behavior was observed in figure 2.6.

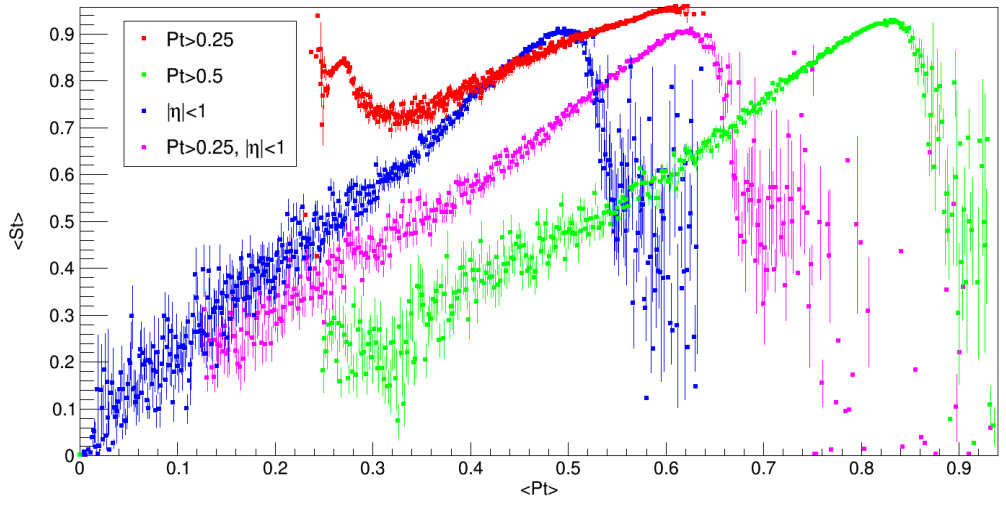

Fig. 2.7: *Mean transverse sphericity vs mean transverse momentum.*